ARTICLE

Core-shell structured microneedles with programmed drug release functions for prolonged hyperuricemia management

Received 00th January 20xx,
Accepted 00th January 20xx

DOI: 10.1039/x0xx00000x

Rui Wang [a,b], Yanfang Sun [c,*], Han Wang [d], Tianqi Liu [a,b], Amin Shavandi [e], Lei Nie [f], Khaydar E. Yunusov [g], and Guohua Jiang [a, b *]

An appropriate non-oral platform via transdermal delivery of drugs is highly recommended for the treatment of hyperuricemia. Herein, a core-shell structured microneedle patch with programmed drug release functions was designed to regulate serum uric acid (SUA) levels for prolonged hyperuricemia management. The patch was fabricated using a three-step-casting method. Allopurinol (AP), an anti-hyperuricemic drug, was encapsulated within the carboxymethyl cellulose (CMC) layer, forming the "shell" of the MNs. The MNs inner core was composed of polyvinylpyrrolidon (PVP) loaded with urate oxidase-calcium peroxide nanoparticles (UOx-CaO_2 NPs). When the as-fabricated core-shell structured microneedles were inserted into the skin, the loaded AP was first released immediately to effectively inhibit the production of SUA due to the water-solubility of CMC. Subsequently, the internal SUA was further metabolized by UOx, leading to exposure of CaO_2 NPs. The sustained release of UOx accompanied by the decomposition of CaO_2 NPs which was contributed to maintaining a state of normal uric acid levels over an extended period. More attractively, the uric acid could be oxidized due to the strong oxidant of CaO_2, which was beneficial to the continuous consumption of uric acid. *In vivo* results showed that the as-fabricated MNs exhibited an excellent anti-hyperuricemia effect to reduce SUA level to normal state within 3 h and maintain normouricemia state for 12 h. In addition, the levels of creatinine (Cr), and blood urea nitrogen (BUN) in serum remained within normal range, and the activities of adenosine deaminase (ADA) and xanthine oxidase (XOD) in the liver were effectively inhabited, mitigating the risk of liver and kidney damages for clinical anti-hyperuricemia management.

Introduction

Hyperuricemia (HUA) is a widespread metabolic disease marked by an elevated level of uric acid and is a risk factor for premature death [1]. Epidemiologic studies revealed that the prevalence of hyperuricemia had increased quickly worldwide in the past few decades, with the aggravation of population aging and lifestyle modification [2,3]. Furthermore, HUA is a hazardous factor for gout, which has been considered as the pathogenesis of cardiovascular disease, diabetic nephropathy, renal dysfunction, hypertension, and metabolic syndrome [4,5]. HUA is mainly caused by renal underexcretion and hepatic overproduction of serum uric acid (SUA). Therefore, the clinical therapeutic strategies for lowering SUA levels mainly act by promoting the uric acid excretion or inhibiting the production of uric acid [6,7]. Allopurinol (AP), a general XOD inhibitor, is the most commonly prescribed agent for treating hyperuricemia by inhibiting the production of uric acid [8,9]. Nevertheless, it can only cover up the symptoms rather than thoroughly cure HUA because it lacks the capability to clear away the existing SUA [10]. In addition, AP is associated with multiple side effects in certain cases, including glomerulonephritis, nephritis, elevated hepatic enzymes, hepatic necrosis, leukocytopenia, purpura, and allergic diseases [11]. Although there is no steep dose-response relationship between AP and its side effects, reducing or delaying the intake dose of AP can reduce its side effects to a great extent. Urate oxidase (UOx) is a key enzyme in SUA metabolism that can oxidize SUA into allantoin and H_2O_2 and eliminate existing SUA [12]. However, UOx is rather unique due to its lack of a co-factor, which is typically required to participate in the catalytic reactions involving O_2 [13].

[a] School of Materials Science and Engineering, Zhejiang Sci-Tech University, Hangzhou, 310018, China
[b] International Scientific and Technological Cooperation Base of Intelligent Biomaterials and Functional Fibers, Hangzhou, 310018, China
[c] College of Life Sciences and Medicine, Zhejiang Sci-Tech University, Hangzhou, Zhejiang, 310018, China
[d] Wenzhou Institute, University of Chinese Academy of Sciences, Wenzhou, China
[e] BioMatter unit-École polytechnique de Bruxelles, Université Libre de Bruxelles, Brussels, Belgium
[f] College of Life Science, Xinyang Normal University, Xinyang 464000, China
[g] Institute of Polymer Chemistry and Physics, Uzbekistan Academy of Sciences, Tashkent, 100128, Uzbekistan
[h] * Corresponding author. E-mail: katherineyfs@zstu.edu.cn (Y. Sun); ghjiang_cn@zstu.edu.cn (G. Jiang)

Electronic Supplementary Information (ESI) available: [details of any supplementary information available should be included here]. See DOI: 10.1039/x0xx00000x

Therefore, it is necessary to enhance UOx reactivity by providing an adequate supplement of O_2. Calcium peroxide nanoparticles (CaO_2 NPs), as a kind of mesoporous nanoparticles, have drawn widespread attention owing to their nontoxicity, low price, environmental-friendly, and high-quality oxygen release properties [14,15]. The O_2 generated by the hydrolysis of CaO_2 NPs not only provides the necessary support for the catalytic decomposition of uric acid by UOx, but also accelerates the breakdown of CaO_2, which contributes to the sustained release of UOx. Additionally, it can function as a solid strong oxidant to oxidize uric acid, thereby achieving the goal of continuous consumption of uric acid [16,17].

A suitable non-oral platform should ideally be designed to avoid side effects and improve drug utilization. Microneedles (MNs) are a transdermal drug delivery system, that can penetrate the stratum corneum of the skin, allowing drugs to enter the systemic circulation through capillaries to achieve therapeutic purposes [18-22]. Therefore, it can eliminate the first-pass metabolism and improve the drug utilization [23]. Additionally, the MNs system provides a safer and painless alternative to subcutaneous injections, which can avoid unexpected side effects and improve the patient's compliance [24,25]. Moreover, compared with traditional transdermal delivery strategies, MNs technology can deliver high molecular weight drugs and increase the drug permeability [26,27]. Hence, MNs technology has received widespread attention and developed rapidly in clinical applications. Recently, a polymer MNs system has been developed by our group for transdermal delivery of AP to acute hyperuricemic mice. An *in vivo* study demonstrated that the AP-loaded MN system can effectively reduce SUA levels, akin to oral administration but with lower side effects, which will be conducive to reducing the adverse reactions and improving the bioavailability of AP. The SUA levels can still be maintained at the therapeutic level (~150 μmol/L) even after 5 h [28]. However, the effective timeframe for regulation SUA levels by this MNs system remains relatively limited, posing a challenge in meeting the daily requirements for long-term SUA level management.

This study developed a core-shell structured microneedle patch with programmed drug release functions to regulate SUA levels for prolonged HUA management and mitigate toxicity-related side effects while maintaining the therapeutic efficacy both *in vitro* and *in vivo*. Carboxymethyl cellulose (CMC), as one of the most promising cellulose, has received extensive attention in biomedical applications due to its excellent water solubility, biodegradability, biocompatibility, and high viscosity [29,30]. Therefore, AP was encapsulated into the CMC layer as the "shell" of MNs, which was supported by polyvinylpyrrolidon (PVP) loaded with urate oxidase-calcium peroxide nanoparticles (UOx-CaO_2 NPs) as the "core" of MNs. When the as-fabricated core-shell structured MNs were inserted into the skin, AP was released immediately to inhibit the production of SUA due to the excellent water-solubility of CMC. Afterwards, the internal SUA could be metabolized by UOx to form allantoin and H_2O_2 upon exposure of the "core" of MNs to skin tissue. The generated allantoin is more easily, absorbed and excreted by renal tubules, and the H_2O_2 could be scavenged due to the potent antioxidant activity of uric acid [31,32]. Subsequently, CaO_2 NPs was exposed as a high-quality oxygen release reagent, and the generated O_2 provides an essential support for the catalytic oxidation of uric acid by UOx. Hence, the sustained release of UOx accompanied by the decomposition of CaO_2 NPs which was contributed to maintaining a state of normal uric acid levels over an extended period. In addition, the uric acid could be oxidized due to the strong oxidant of CaO_2, which was also beneficial to the continuous consumption of uric acid (Figure S1). In addition, a hyperuricemia model was established to assess the effect of inhibiting SUA levels *in vivo*. Biochemical indicators, such as creatinine (Cr), blood urea nitrogen (BUN) and the activities of adenosine deaminase (ADA) and xanthine oxidase (XOD) in the liver, were evaluated for comparison with the oral treatment route.

Experimental

Chemicals and reagents

Calcium chloride dihydrate ($CaCl_2 \cdot 2H_2O$), hydrogen peroxide (H_2O_2, 30 wt.%) and ammonia solution ($NH_3 \cdot H_2O$, 25~28 wt.%) were purchased from Aladdin Chemistry Co. Ltd (Shanghai, China). Polyvinylpyrrolidon (PVP, K88-96, Mw = 1300 kDa and K30, Mw = 58kDa), polyvinyl alcohol (PVA, 1788 type, alcoholysis = 87.0-89.0%), carboxymethyl cellulose (CMC, Mw = 90,000), urate oxidase (UOx, ≥20 U/mg), allopurinol (AP), potassium oxonate (PO) and hypoxanthine (HPT) were provided by Macklin Biochemical Co., Ltd (Shanghai, China). Assay kits for serum uric acid (UA), serum creatinine (SCr), blood urea nitrogen (BUN), xanthine oxidase (XOD), and adenosine deaminase (ADA) activity were obtained from Elabscience Biotechnology Co., Ltd (Wuhan, China). CaO_2 nanoparticles (NPs) were synthesized based on a previously reported method [33].

Preparation of UOx-CaO_2 nanoparticles

UOx-CaO_2 was prepared by mixing 500 μL Tris-HCl buffer solution (pH = 8.4) containing 20 mg of UOx with CaO_2 ethanol solution (1 mg/mL, 10 mL) and stirring at room temperature for 12 h. Afterwards, the samples were obtained by centrifugation at 10,000 rpm for 10 min and washing with ethanol three times. The obtained UOx-CaO_2 samples were resuspended in ethanol and stored at 4 ℃ for further use. Additionally, the encapsulation efficiency (EE) and loading capacity (LC) of UOx were calculated.

Characterization

The surface morphology and size of nanoparticles and MNs were analyzed by scanning electron microscopy (SEM, Vltra55, Zeiss, Germany) and transmission electron microscopy (TEM, JEOL, JSM-2100, Japan). Particle size and zeta potential measurements were conducted by Malvern Zetasizer Nano ZS system (Malvern Instruments, Worcestershire, UK). N_2 absorption-desorption isotherms were estimated by the

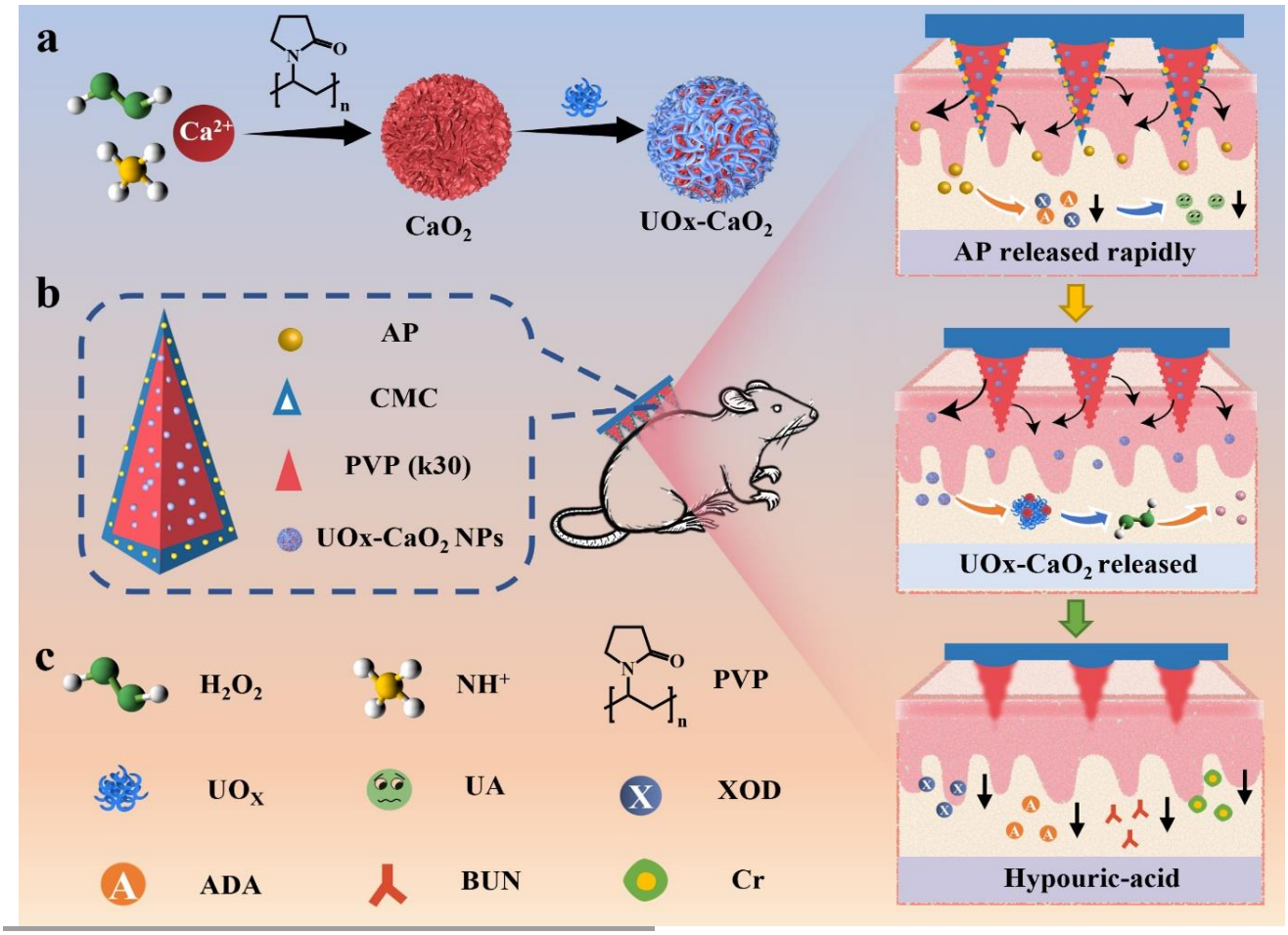

Scheme 1. Schematic illustration of core-shell structured MNs for synergistic therapy against hyperuricemia

Brunauer-Emmett-Teller (BET) method using a Quantachrome specific surface area and pore size analyzer (BeiShiDe Instrument Technology (Beijing) Co., Ltd, ps2-1195, China) to identify the specific surface area, pore size distribution and pore volume of the samples. XRD spectra were recorded on an X-ray photoelectron spectroscopy (K-Alpha, Thermo Fisher Scientific). Fourier transform infrared (FTIR) spectra were implemented on a Nicolet 5700 FTIR spectrometer (Thermo Electron Corporation, USA), and the spectra were collected in the range of 4000-400 cm^{-1}.

Design and fabrication of the core-shell structured MNs

A three-step-casting micromolding approach was used to fabricate the core-shell structured MNs. The AP loading in shell layer can be precisely controlled by adjusting the concentration of AP, and the dose of AP in the shell matrix was determined by an UV-vis spectrophotometer (Figure S2). Therefore, 20 mg AP was dispersed in 10 mL CMC aqueous solution (6%), and ~100 μL of this mixture was pipetted onto the PDMS mold cavities by vacuuming to form the outer layer of the MNs. Subsequently, the mold was dried in a vacuum drying oven (37°C) for 12 h to harden the "shell" layer of MNs. After drying overnight, 10 mg UOx-CaO_2 NPs were mixed with PVP (k30, 10 mL, 60%) ethanol solution, and ~100 μL of the above mixture was filled into the microcavities of the mold to form the "core" layer of MNs. The backing layer aqueous solution (PVA/PVP, 1:1, 20%, w/v) was then filled into the mold and dried in a vacuum drying oven (37°C). The core-shell structured MNs labeled as S/C-MNs were obtained after demolding. Similarly, a shell layer loaded with AP MNs (S-MNs) and a core layer loaded with UOx-CaO_2 MNs (C-MNs) were fabricated using the same method. The S-MNs with 0.2 mg AP in an MN patch were fabricated by pipetting ~100 μL AP@CMC solution into PDMS mold cavities (20 × 20 arrays) to form the "shell" layer of MNs, and then the PVP (k30, ~100 μL, 60%) ethanol solution was filled into the mold after the "shell" layer was dried overnight in a vacuum drying oven (37°C). C-MNs with 0.1 mg UOx-CaO_2 NPs in an MN patch were constructed using a CMC aqueous solution (6%) layer as the "shell" layer and a PVP (k30, 10 mL, 60%) ethanol solution loaded with UOx-CaO_2 NPs (10 mg) as the "core" of MNs.

To verify the core-shell structure, fluorescent-dyed MNs with green FITC- labeled shells and red R6G-labeled cores were also fabricated using the same method, and fluorescence images were captured by fluorescence microscope (ZEISS, Axio Vert.A1, Germany) and laser scanning confocal microscopy (CLSM, C2, Nikon Corporation, Japan). To investigate the insertion properties, the mechanical strength of the MNs was

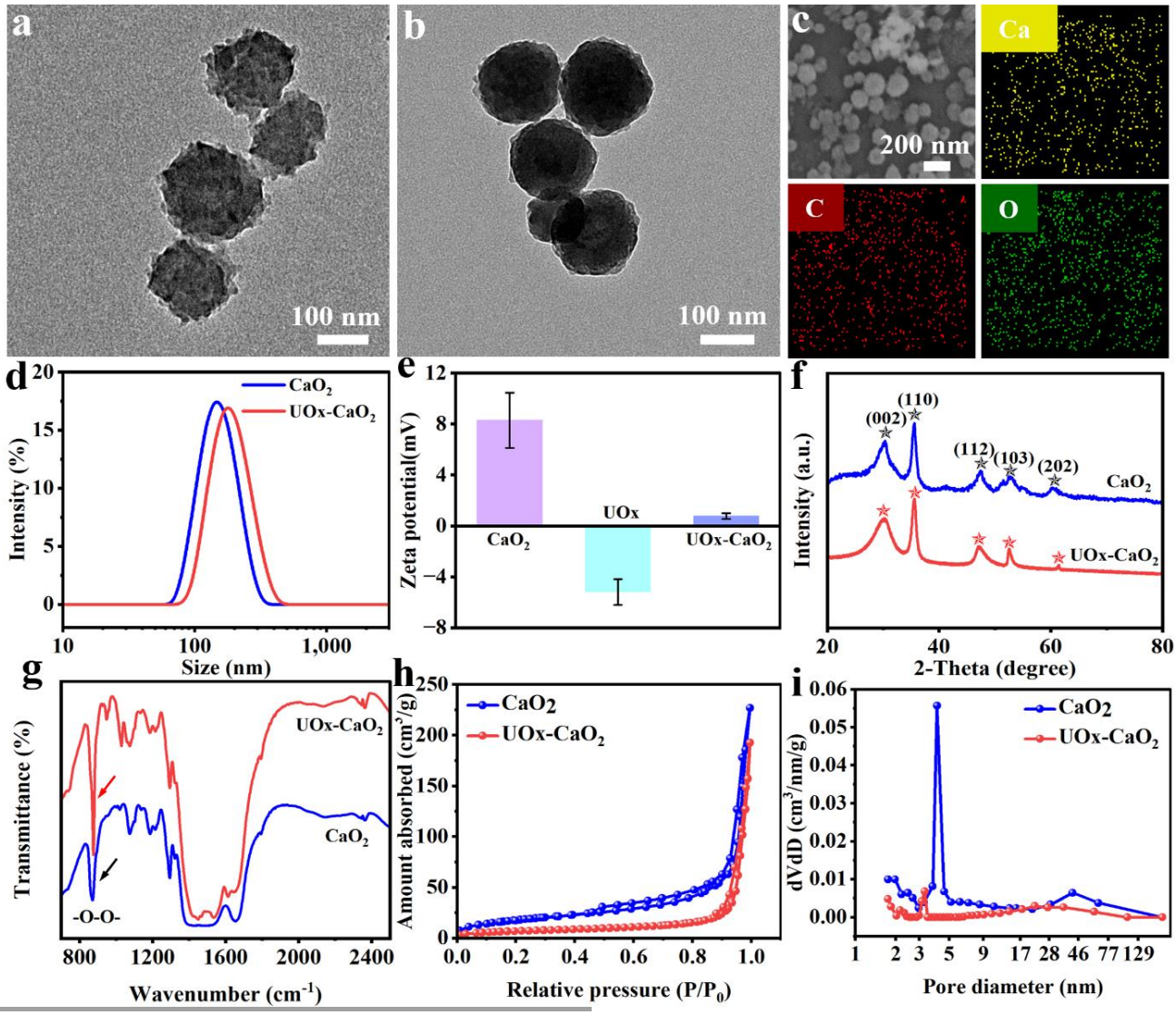

Figure 1. TEM images of (a) CaO_2 and (b) UOx-CaO_2. (c) Elemental mapping of UOx- CaO_2. (d) Hydrodynamic sizes and (e) zeta potential of CaO_2 and UOx- CaO_2. (f) XRD patterns and (g) FTIR spectrum of CaO_2 and UOx-CaO_2. (h) N_2 adsorption-desorption isotherms and (i) corresponding pore sizes of CaO_2 and UOx-CaO_2.

measured using a universal testing machine (5943 MicroTester, Instron, America). To evaluate the drug penetration performance, the as-prepared fluorescent-dyed MNs were pierced vertically into the excised mouse skin by thumb pressure and kept for 2 min. The mouse skin site inserted by MNs was embedded in paraffin and sliced into 6 μm sections, followed by hematoxylin and eosin (H&E) staining. The H&E staining sections were visualized by a fluorescence microscope.

AP release *in vitro*

To assess the release kinetics of AP from the S/C-MNs, a Franz diffusion cell was applied for *in vitro* transdermal diffusion detection. Fresh mouse skin inserted with S/C-MNs patch was fixed over the receiving chamber containing 25 mL PBS solution, followed by incubating in the water bath at room temperature under magnetic stirring at 400 rpm. At the predetermined time point, 3 mL aliquots were removed and complemented with the equivalent volume of blank PBS. The drug release efficiency was ultimately determined by an ultraviolet-visible spectrophotometer (UV, TU-1901, Beijing Purkinje General Instrument Co., Ltd, China).

Biosafety of MNs *in vitro* and *in vivo*

Different concentrations of CaO_2 solution were incubated in 96-well culture plate against 3T3 and L929 cells to assess the cytotoxicity of CaO_2 NPs. After incubation for 24 h, the cell viability was determined by a MTT method. The viability of L929 cells was also employed to evaluate the cytocompatibility of as-fabricated MNs. The live/dead staining of L929 cells co-cultured with the supernatants of MNs for 12, 24 and 48 h was conducted and recorded by a CLSM. Additionally, given the long-term nature of the treatment, the inflammation responses of skin section treated with prepared MNs for 12 h

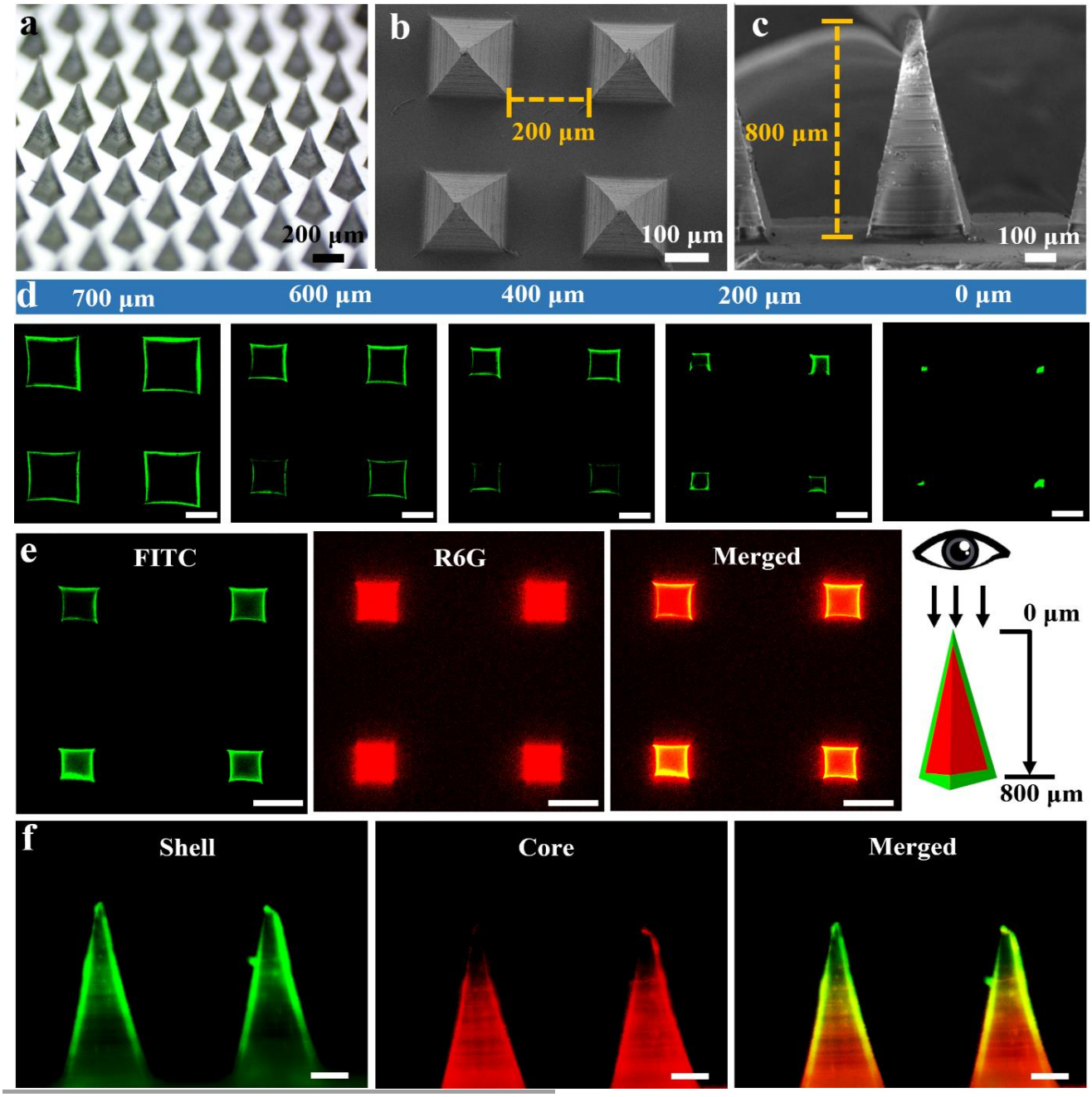

Figure 2. Stereomicroscope (a) and SEM (b and c) images of MNs. (d) Fluorescence images of cross-sections of prepared MN with shells obtained by CLSM along z axis from tip to base (scale bar:100 μm). (e) Representative microscopy images of cross-section of a core-shell MN at depth of 500 μm, showing the green shell labeled with FITC and the red core labeled with rhodamine 6G (scale bar: 200 μm). (f) Fluorescence microscope images of vertical-section of a core-shell MN (scale bar: 200 μm).

and 24 h were analyzed by IL-6 immunohistochemistry staining.

Hyperuricemia management *in vivo*

Thirty-six healthy ICR mice (6-8 weeks old, 20-22g) were provided by Wenzhou Institute, University of Chinese Academy of Sciences (Wenzhou, Zhejiang, China). Mice were housed under a controlled environment (22-26°C, 40-70% humidity, 12 hours light/dark cycle) with free access to standard chow and water. All the in vivo experimental procedures were conducted and complied with the Guide for the Care and Use of Laboratory Animals of Wenzhou Research Institute, Chinese Academy of Sciences (Ethics Code Permit WIUCAS23051802).

After one week of acclimatization, mice were randomly divided into six groups (n = 6): normal control group (control); hyperuricemia model group (model); oral group (administrated AP by gavage); MNs-1 group (administrated by S-MNs with 0.2 mg AP in an MNs patch); MNs-2 group (administrated by C-MNs with 0.1 mg UOx-CaO_2 NPs in an MNs patch); MNs-3 group (administrated by S/C-MNs with 0.2 mg AP and 0.1 mg UOx-CaO_2 NPs in an MNs patch). Except for the normal control group, mice in other groups were injected with hypoxanthine (150

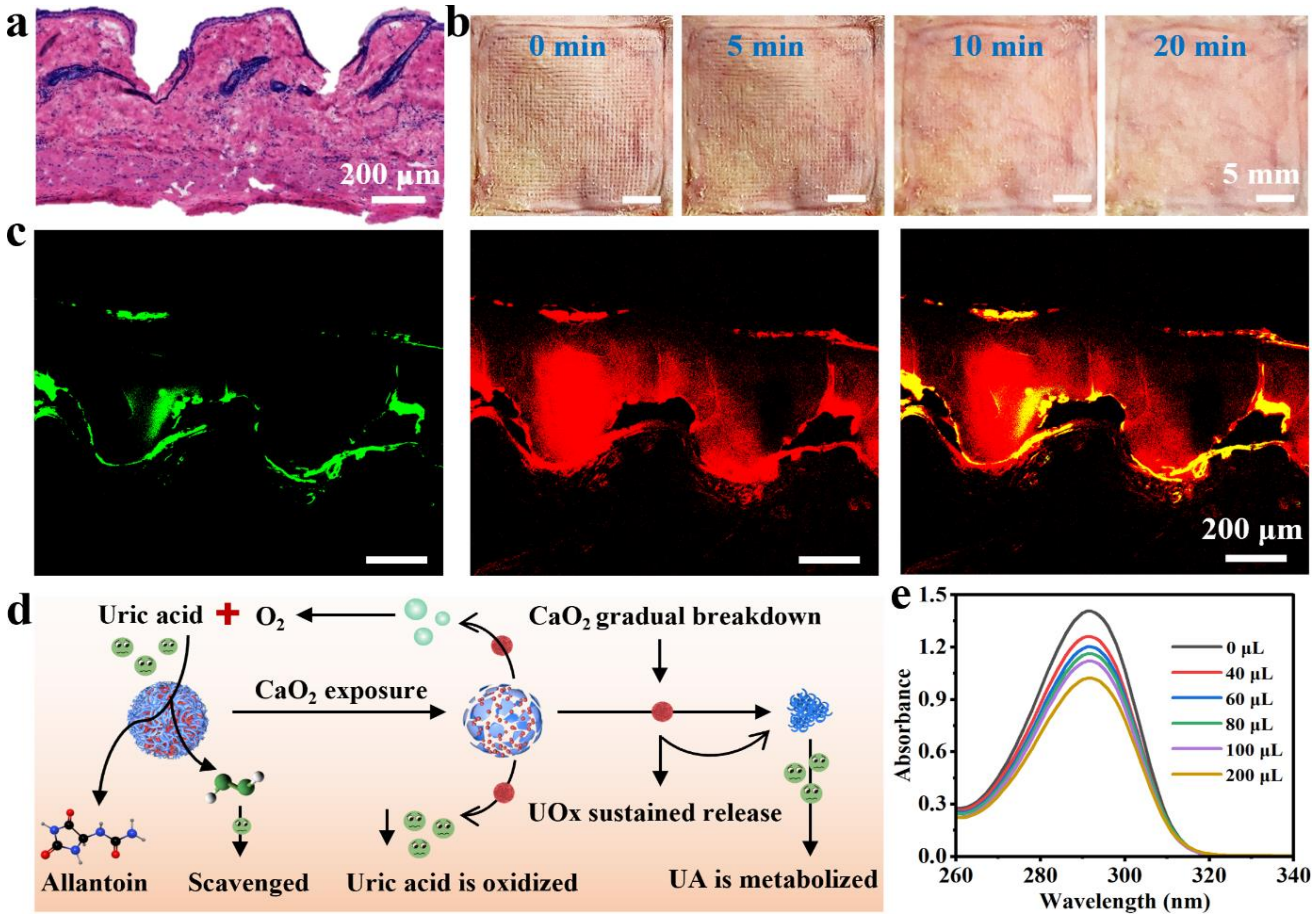

Figure 3. (a) Image of H&E staining of mouse skin after MNs application. (b) The needle spots on the mouse skin surface after the insertion and removal of core-shell MN patch, and the skin recovery over time after MNs application. (c) Fluorescence images of cross-sectional excised mouse skin inserted by fluorescent core-shell MNs. (d) Mechanism scheme of SUA modulation by the core layer of MNs with encapsulation of UOx-CaO_2 NPs. (e) The UV-visible absorption spectra of UA with increased concentration of CaO_2.

mg/kg) intraperitoneally and potassium oxyacetate (250 mg/kg) subcutaneously once a day for 15 days to establish hyperuricemia models. On day 15, mice in the control group were treated with 0.9% sodium chloride aqueous solution, whereas mice in the other groups were administered by the corresponding interventions after modeling. Blood was taken from the orbit at predetermined intervals and placed in a refrigerator at 4℃ overnight to collect serum. The levels of serum uric acid (SUA), blood urea nitrogen (BUN), and serum creatinine (SCr) were assessed using the appropriate biochemical assay kit. After the mice were euthanized, organ tissues were excised for biochemical and histological examination. The XOD and ADA activities in the supernatants of hepatic tissue homogenates were measured using a standard biochemical assay kit. The retrieved tissues were embedded in paraffin and sliced into 5 μm thick sections for histological analysis. The obtained sections were stained with hematoxylin and eosin (H&E), and the general morphological was evaluated under an optical microscope.

Statistical analysis

All quantitative data presented in this study are the means ± standard deviation (SD). Statistical significance was determined by one-way ANOVA using GraphPad Prism 8.0 (GraphPad Software, Inc., San Diego, CA). P-values < 0.05 were considered statistically significant differences.

Results and discussion

Preparation of UOx-CaO_2 NPs

AP is extensively applied as an outstanding clinical anti-hyperuricemia drug. However, the clinical application of AP is limited due to its multiple side effects. Herein, a core-shell structured MNs with programmed drug release functions is designed to regulate SUA levels for prolonged hyperuricemia management (Scheme 1). Firstly, CaO_2 NPs are synthesized by the reaction of $CaCl_2{\cdot}2H_2O$ with H_2O_2 in ethanol using PVP as a stabilizer, exhibiting a uniform size distribution (Figure S3). The elements Ca, C, O and N can be detected in these nanoparticles (Figure S4). TEM images display that the particles have a spherical shape with an average diameter of about 128 nm (Figure 1a). The hydrodynamic size and zeta potential of CaO_2 NPs are 134.71 ± 0.87 nm and 8.29 ± 2.17 mV tested by the dynamic light scattering (DLS) measurements (Figure 1d and 1e). The XRD pattern of CaO_2 NPs shows

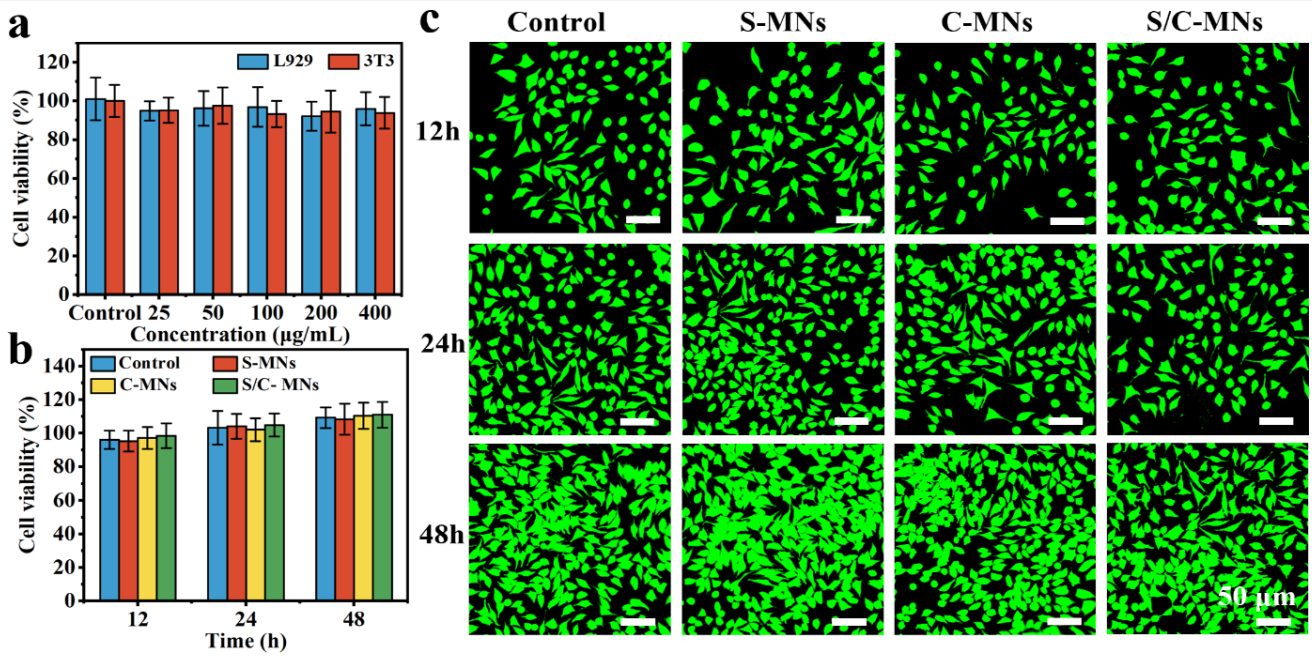

Figure 4. MTT assay of 3T3 and L929 co-cultured with CaO_2 solution (a) and prepared MNs (b). (c) Live/dead staining of L929 cells co-cultured with shell-only, core-only, and core-shell MNs.

characteristic peaks at 2θ values of 30.2, 35.6, 47.4, 53.0, and 60.4, which matched well with the standard diffraction peaks (002), (110), (112), (103) and (202) of CaO_2 (JCPDS No. 03-0865) (Figure 1f) [34]. FT-IR was utilized to further assess whether CaO_2 NPs were successfully prepared by analyzing the characteristic absorption peak of peroxide groups. The absorption bands at 881 cm^{-1} corresponded to the characteristic peaks of peroxide bonds (O–O), indicating that CaO_2 has been successfully prepared (Figure 1g). The N_2 adsorption-desorption isotherm curves and pore size distribution plots indicate that the specific surface area, pore volume, and an average pore size of CaO_2 NPs are 65.95 m^2/g, 0.33 cm^3/g and 19.95 nm, respectively (Figure 1h and 1i). The loading of UOx is analyzed by UV-vis spectrophotometry. According to the standard curve (Figure S5), the encapsulation efficiency and loading capacity are 62.41% and 39.4%, respectively. After loading of UOx, the morphology of UOx-CaO_2 NPs is close to that of CaO_2 NPs (Figure 1b). Figure 1c shows the elemental mapping of UOx-CaO_2 NPs, demonstrating the uniform distribution of Ca, C, and O elements. The average hydrodynamic diameter slightly increased from 134 to 154 nm, which is confirmed by DLS measurement (Figure 1d). The zeta potential of CaO_2 is +8.29 mV, but it is decreased to 0.78 mV after loading of UOx (-5.18 mV), indicating that UOx is successfully loaded into CaO_2 NPs (Figure 1e). Moreover, the decreased specific surface area (25.51 m^2/g), pore volume (0.25 cm^3/g), and pore size (6.36 nm) further confirmed the successful construction of UOx-CaO_2 NPs (Figure 1h and 1i). In addition, the distinct diffraction peaks of UOx-CaO_2 in XRD pattern are consistent with those of CaO_2 NPs (Figure 1f), and the characteristic absorption peaks of peroxide groups can also be observed appear in the FTIR spectrum of UOx-CaO_2 (Figure 1g), indicating that there is no effect on the crystal structure of CaO_2 after loading of UOx.

Fabrication of the core-shell structured MNs

To achieve a prolonged anti-hyperuricemia effect, a new core-shell structured MNs system with programmed drug release functions was designed to regulate SUA levels for prolonged hyperuricemia management. The "shell" layer of MNs consists of CMC and AP, in which the rapid dissolution of CMC offers a rapid release of AP into the blood. The internal SUA could be further metabolized by UOx upon reaction with the "core" of MNs with skin tissue, resulting in a prolonged anti-hyperuricemia effect. The core-shell structured MNs are fabricated by three-step-casting method (Figure S6). The representative core-shell structured MNs arranged in a 20 × 20 array are observed under stereomicroscope and SEM (Figure 2a-c), which displayed predicted specific periodic pyramid-like structures with ~800 μm in height and ~200 μm in base diameter (Figure S7). Figure 2d shows the fluorescence images of cross-sections of MNs, and green fluorescence square rings can be found at different height within the shell-defined region. Meanwhile, a solid red fluorescence signal can be observed in the inner of MNs (Figure 2e). The vertical-section image of representative MNs was recorded by CLSM, showing a green-fluorescent shell, a red-fluorescent core, and a combination of the red and green fluorescent merged images, which further validated the core-shell structure of MNs (Figure 2f).

Insertion of the core-shell structured MNs *in vitro*

The mechanical strength of MNs plays a significant role in skin penetration and insertion. To investigate whether the core-shell structured MNs can tolerate the required compressive force for skin insertion, the pressure-compression

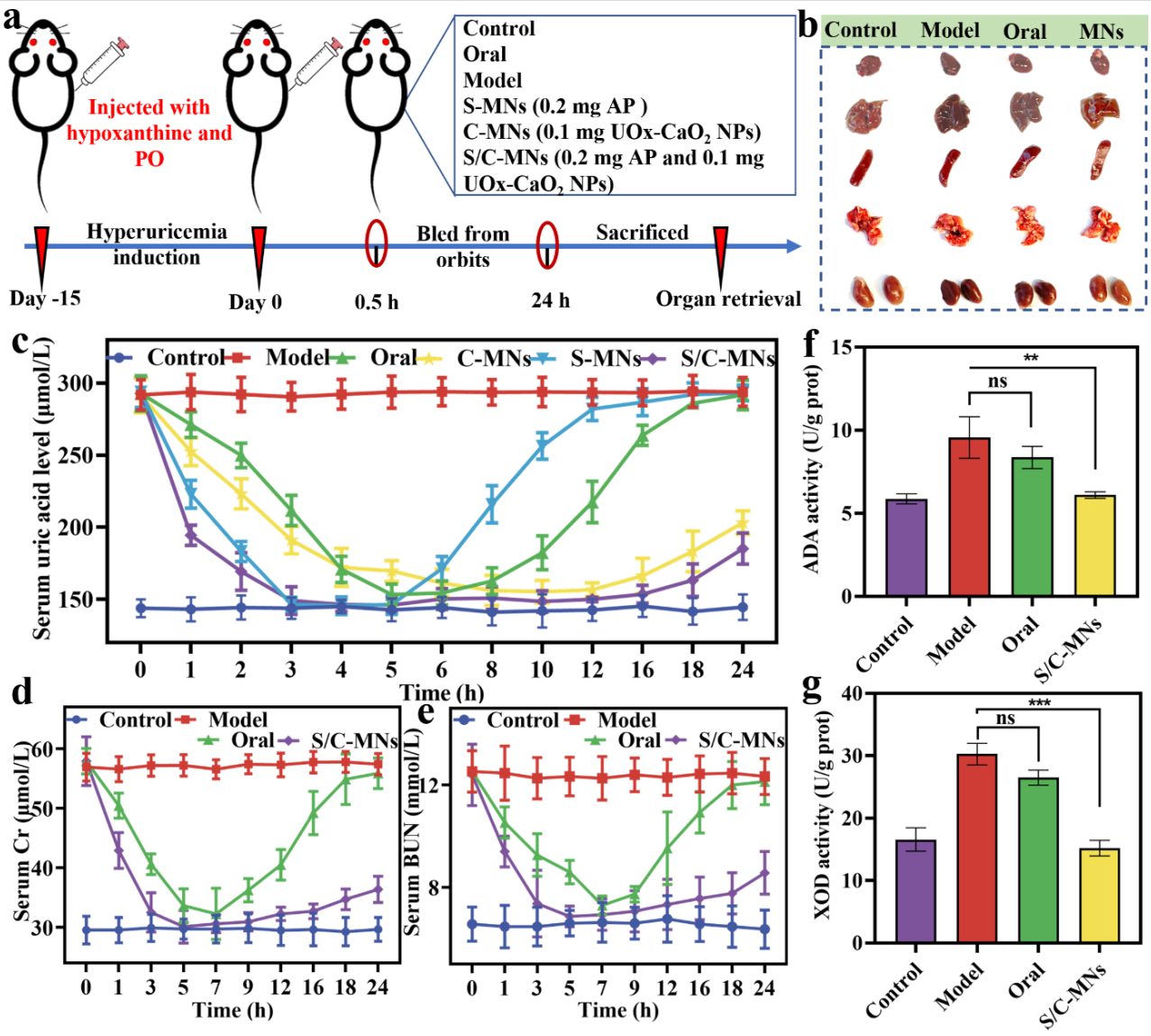

Figure 5. (a) The *in vivo* experiment process for the modulation of SUA levels. (b) Images of heart, liver, spleen, lung, and kidneys organs retrieved from the treated mice. The SUA (c), SCr (d) and serum BUN (e) levels of the mice, and the XOD (f) and ADA (g) activities of the liver in each group.

tests were performed by a universal testing machine (Figure S8). The compression test revealed that the failure force of prepared MN patches is significantly higher than that needed for mucosa penetration [35]. The maximum tolerated compressive force of as-fabricated core-shell structured MNs is approximately 0.22 N per needle with displacement at 500 μm, which is sufficient to penetrate into human skin without breaking, while the strength of S-MNs is only 0.09 N per needle with displacement at 500 μm. In addition, the isolated skin tissues from mice are treated with core-shell structured MNs, and then H&E staining was performed. As shown in Figure 3a, the MNs successfully can be penetrated the stratum corneum, suggesting high applicability of MNs in *ex vivo* skin. And the difference size between the microchannel in the histological image and the real microneedle is due to the known skin surface deformation during the insertion of MNs [36] An array of needle spots can also be observed on the skin surface after the removal of MNs patch, which is attributed to the good mechanical strength of the as-prepared MNs (Figure 3b). These needle spots can slowly vanish after removing the MNs patch and almost completely disappear after 20 min. This suggests that the administration site of the skin can also be returned to its initial state within a short time using MNs patches, and no skin allergic and irritation reaction can be observed. They are suitable for the frequent administration of medicines via the transdermal route. To further estimate the insertion ability of the core-shell structured MN, fluorescent-dyed MNs were applied to the excised mice dorsal skin. Many microchannels with a depth of ~400 μm can be observed, suggesting that MNs can be efficiently inserted into the skin (Figure 3c). In addition, in the fluorescence microscope field, the red fluorescence of R6G can be found in the inner microchannels and the green fluorescence of FITC is dispersed in the outer-ring of microchannels and both overlapped to

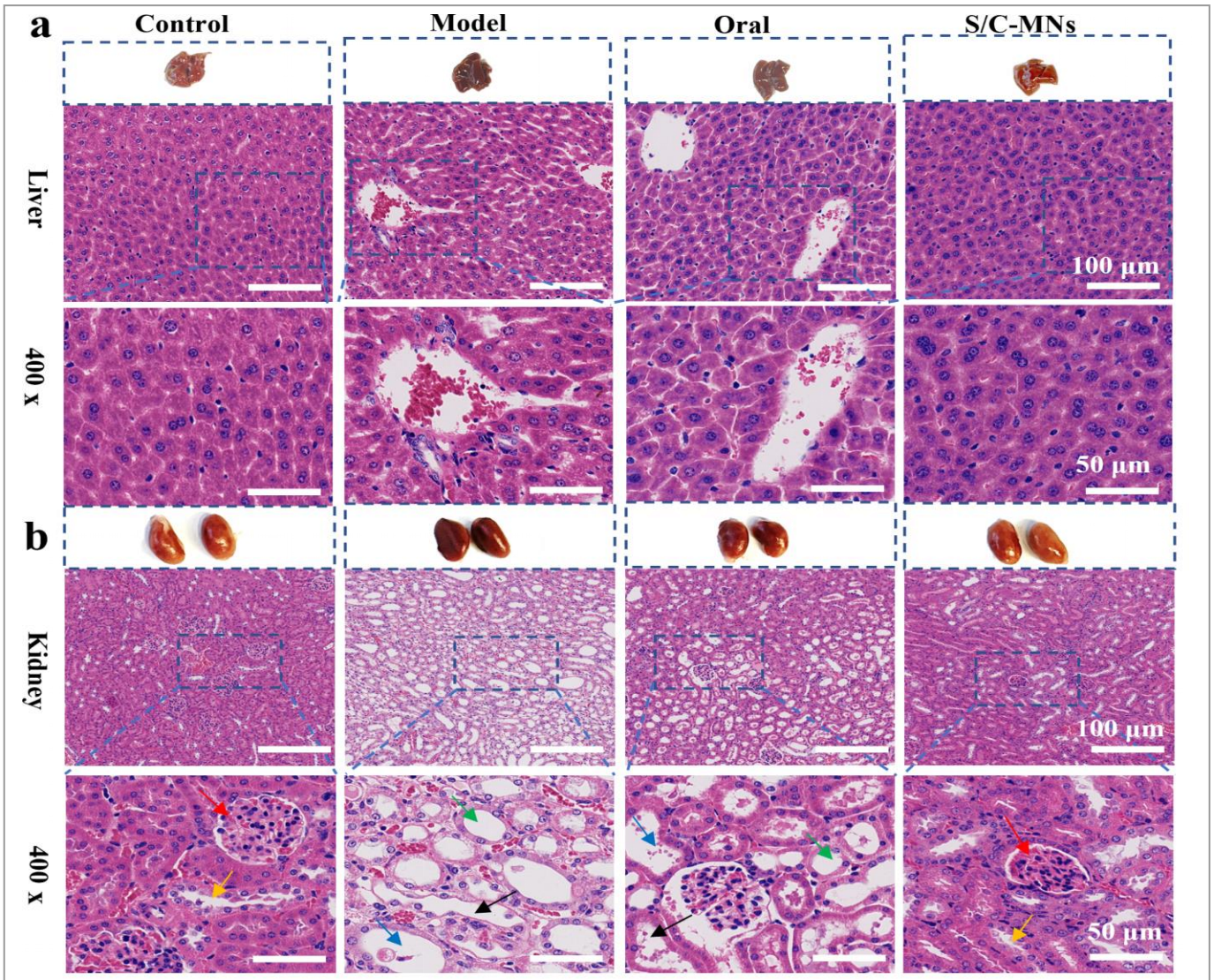

Figure 6. H&E staining images of tissue slices of the liver (a) and kidney (b) from treated mice (red arrow: normal glomerulus morphology, yellow arrow: complete brush border structure, green arrow: dilatation of renal tubule, blue arrow: renal interstitial inflammatory cell infiltration, black arrow: the disappearance of the brush border).

show a yellow fluorescence shell, further confirming the core-shell structure of the as-fabricated MNs.

***In vitro* drug release and underlying mechanism**

To assess the actual transdermal release of AP, a transdermal drug release system was set up via a transdermal diffusion apparatus. The S/C-MN patch was applied to the excised fresh mouse skin by thumb pressure and then fixed over a receptor chamber containing 25 mL of PBS solution. 3 mL solution was taken out from the sampling port at timed intervals for ultraviolet measurement. As shown in Figure 4d, the cumulative release percentage reached ~78% within 2 h and further increased to ~98% after 4 h due to the excellent water solubility of CMC (Figure S9). After the dissolution of the MN shell layer, the core layer of MNs with encapsulation of UOx-CaO_2 NPs will be exposed to the microenvironment of skin tissue.

The possible mechanism of SUA modulation by UOx-CaO_2 NPs was depicted in the Figure 3d. Firstly, UA can be oxidized by UOx to allantoin and H_2O_2. The generated allantoin is more easily absorbed and excreted by renal tubules [37], and the injury caused by H_2O_2 generation can be attenuated due to the high antioxidant activity of UA [30,31,38], which is further confirmed by the shifted absorption peak of UA with the increasing concentration of H_2O_2 (Figure S10). Afterwards, CaO_2 NP is exposed as a high-quality oxygen release reagent, and the generated O_2 provides an essential support for the catalytic oxidation of uric acid by UOx. In addition, the UA can also be oxidized by CaO_2 due to its potent oxidant activity, which is confirmed by decreased intensity of the absorption peak of UA with increasing CaO_2 concentration (ranging from 0 to 200 μL) (Figure 3e).

***In vitro* cytotoxicity**

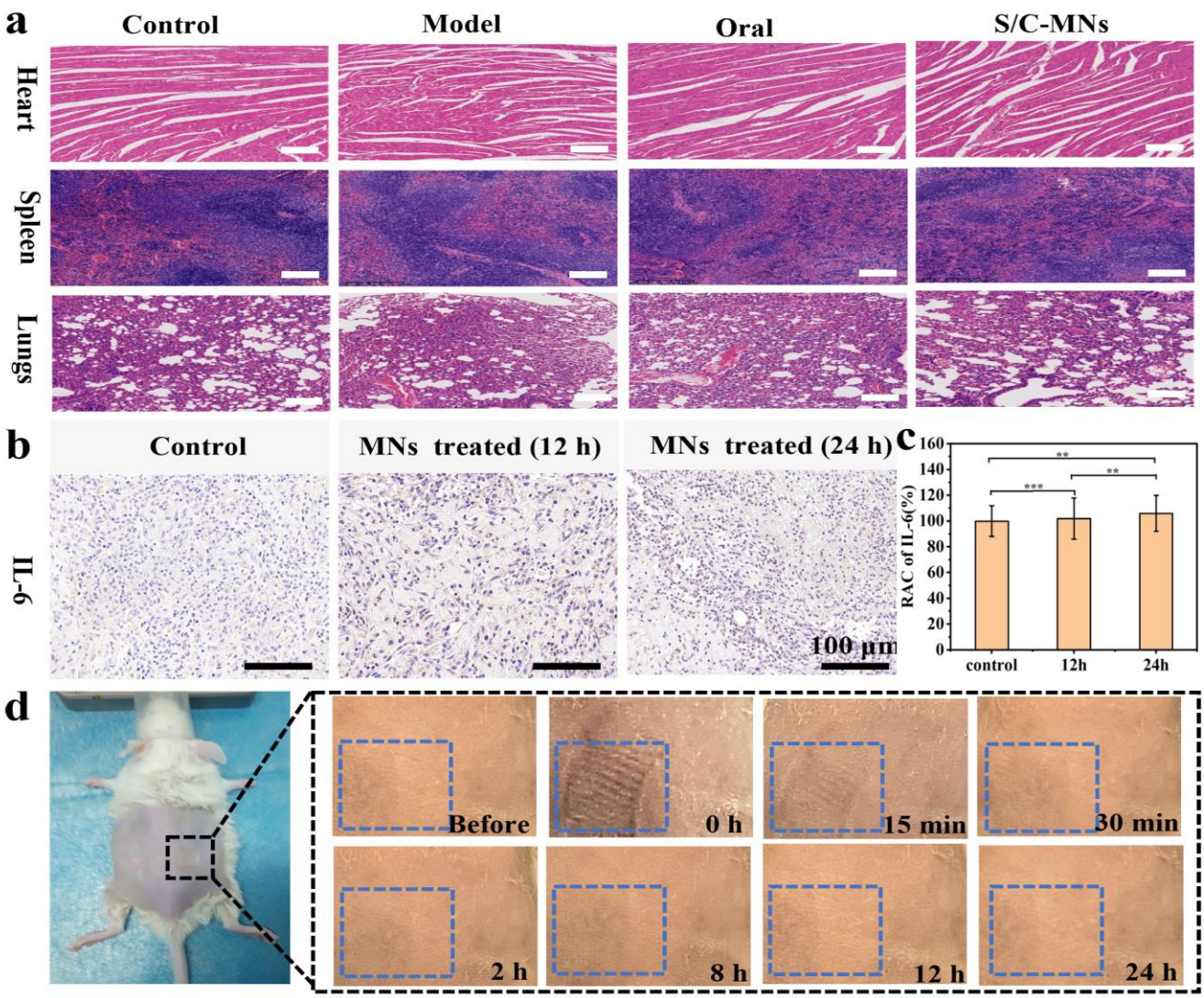

Figure 7. (a) H&E staining images of tissue slices of the heart, liver, spleen and lung. Immunohistochemistry staining images (b) and (c) the quantitative analysis of pro-inflammatory IL-6. (d) Skin recovery at administration sites of healthy mice with the treatments of a core-shell microneedle patch.

To evaluate the cytotoxicity of CaO_2 NPs, different concentrations of CaO_2 solution were co-cultured with L929 and 3T3 cells. The results reveal that there are almost no differences in cell survival rate with CaO_2 concentration ranging from 0 to 400 μg /mL, and the cell viabilities are higher than 95%, indicating the low cytotoxicity of CaO_2 NPs (Figure. 4a). Meanwhile, the biocompatibility of as-fabricated MNs patch was also evaluated by co-culture of MNs matrix (100 μg/mL) and L929 cells. As shown in Figure 4b, the cell viabilities of L929 cells are higher than 90% for shell-layer, core-layer, and core-shell MNs matrices after co-culture for 12h, and they have a slight increase after co-culture for 24 and 48h, indicating the negligible cytotoxicity of MNs matrix. Live/dead staining images of L929 cells co-cultured with MNs matrix for 12, 24 and 48h are shown in Figure 4c. The cell density can be increased with the prolongation of co-culture time, and dead cells are almost undetected even after 48 h.

Regulation of SUA levels *in vivo*

To evaluate the regulation of SUA levels *in vivo*, a hyperuricemia mice model was established by a previously reported method with a slight modification [39]. The comprehensive process for *in vivo* treatment is depicted in Figure 5a. The mice were divided into six groups randomly: (1) control group; (2) model group; (3) oral group; (4) MNs-1 group; (5) MNs-2 group; and (6) MNs-3 group. The SUA levels of treated mice were monitored over time following administration. As shown in Figure 5c, the SUA levels of mice in the control group with a healthy state (~142 μmol/L), while, the model group with hyperuricemia maintained a higher SUA level (~293 μmol/L) for at least 24 h, indicating the successful establishment of a chronic hyperuricemia model. After oral administration of AP (0.2 mg), the SUA levels slowly decreased to ~146 μmol/L within 6 h and maintained for ~3 h under ~160 μmol/L. In the case of MNs-1 group (administrated by S-MNs

with 0.2 mg AP in an MNs patch), the SUA levels can be decreased to a normal state within 3 h, faster than that of the oral group due to the water-solubility of CMC, which accelerates the drug release from shell layer of MNs. The SUA levels can be maintained for ~3 h under ~160 μmol/L which is close to the oral administration. The mice in MNs-2 group that treated by C-MNs with 0.1 mg UOx-CaO_2 NPs in an MNs patch shows a delayed decrease in SUA levels owing to the slowly decomposition of CaO_2 NPs. The SUA levels decrease to ~152 μmol/L after administration for 6 h, and they can be kept at a normouricemia state for almost 8 h, longer than that of pure AP treatment through oral or MNs delivery route. This can be attributed to the oxidation of SUA in the presence of UOx and the high sensitivity of CaO_2 to UA. The above results imply that the integration of AP and UOx-CaO_2 has synergistic effect. To verify the synergistic effect, the SUA levels of the mice treated by shell-core structured MNs were constantly monitored up to 24 h. As shown in Figure 5c, the SUA levels rapidly decreased to ~142 μmol/L within 3 h, and then remained consistent within the normouricemia range for more than 12 h. Even after administration for 24 h, the SUA level was slightly increased to ~180 μmol/L, showing a rapid and prolonged anti-hyperuricemic effect.

Immunohistochemical tests

SCr and BUN are two important indicators of renal dysfunction [40-42]. To verify the nephroprotective effect of the as-fabricated core-shell structured MNs, the SCr and BUN levels were determined by standard Cr and BUN biochemical assay kits. As expected, the SCr level of mice treated with core-shell structured MNs shows a remarkable decrease within 5 h and maintained lower levels even after administration of 24 h, suggesting an excellent protective effect on renal function (Figure 5d). However, after treatment with oral AP, the SCr level displays a rapid decrease in the first 7 h and then gradually returns to its initial state within the following 17 h. The SCr level is close to the model group after administration of 24 h. The BUN levels in all groups exhibit a similar trend, as shown in Figure 5e. These results indicate that as-fabricated core-shell structured MNs has a more promising effect for hyperuricemia management.

ADA and XOD, mainly present in the liver, are pivotal enzymes in purine catabolism. ADA plays a critical role in transforming adenosine to inosine, which can be converted into hypoxanthine and xanthine [43,44]. XOD directly contributes to the UA production by oxidizing hypoxanthine and xanthine into UA [45,46]. Herein, hepatic XOD and ADA activities were tested to explore the mechanism of SUA regulation at the end of the experiment. Figure 5f and 5g shows the results of XOD and ADA activities after treatment. The XOD and ADA activities in model group are significantly higher than those in the healthy group due to the high SUA levels. After treatment with oral AP, both XOD and ADA activities were decreased slightly, showing a short-term enzyme inhibition effect. However, the XOD and ADA activities in the core-shell structured MNs group exhibit similar levels compared with those in control group, implying a strong inhibition effect on ADA and XOD. These results suggest that the as-fabricated core-shell MNs can effectively reduce the production of SUA and liver damage by inhibition the activities of XOD and ADA. At the end of treatment for 24 h, the main organs, heart, liver, spleen, lung, and kidney tissues, were retrieved (Figure 5b). No significant drastic liver and kidney changes are found in the as-fabricated core-shell MNs groups compared with the control group, suggesting no remarkable liver damage and renal impairment by MNs administration. In contrast, acute liver and kidney damage can be founded in the model group, which also confirmed by the increase of SCr and ADA levels. Traditional oral drug administration also showed liver toxicity due to the first-pass effect and slow clearance. Hence, the MNs-mediated strategy developed in this study has the potential to be used as an attractive anti-hyperuricemia treatment with lower damage and toxicity and a longer therapeutic effect.

Histopathological analysis

Histopathological analyses of the treatment groups were performed to observe organ features and identify the effects of each group. H&E-stained organs samples from each group were observed with optical microscopy. As shown in Figure 7a, no tissue lesions are found in the heart, lung, and spleen in any of the groups. However, the liver cell of the model group shows severe liver cell edema with steatosis, punctate necrosis, and extensive lymphocyte infiltration, indicating severe liver damage development in hyperuricemic mice [10]. Moreover, the liver cell edema with steatosis can also be observed in oral administration group due to the first-pass effect [47-49]. There are no significant abnormalities in the liver cells in the core-shell structured MNs administration group, suggesting the negligible liver damages (Figure 6a).

The kidney is an important organ for UA excretion, and further evidence has suggested that an increase of UA level is a predictive indicator for subjects with end-stage kidney disease (ESKD) and chronic kidney disease (CKD) [50,51]. To assess the potential kidney damage, the H&E staining of kidney tissues was conducted to investigate the effect of MNs administration on renal ultrastructure changes. As shown in Figure 6b, the kidney tissue sections of the control group shows a natural histological structure with normal glomeruli and renal tubules, and without evidence of inflammation. In contrast, the hyperuricemic model group exhibits symptoms with the glomeruli swelling, tubular dilation, inflammatory cell infiltration, and mild Bowman's capsule expansion, indicating severe renal tissue damage development in hyperuricemic mice. In addition, the extensive renal impairment can also be observed in oral administration group, which is confirmed by tubular dilatation vacuolization, and infiltration of inflammatory cells. However, abnormal pathological changes

do not appear in the MNs administration group, suggesting the alleviation for renal histopathological damages.

Additionally, given the long-term nature of the treatment, the local irritation and inflammation responses of MNs administration were further evaluated. The upregulation of IL-6 expression indicates an enhanced inflammatory response, which may limit the clinical application of MNs [52,53]. Therefore, the IL-6 immunohistochemistry staining of skin sections treated with prepared MNs for 12 and 24 h were performed. As shown in Figure 7b and 7c, the skin slice of MNs treated for 12 h shows almost similar levels of pro-inflammatory IL-6 expression as compared to the control group. Moreover, the IL-6 levels only increased by 6.2% even after 24 h of MNs treatment, indicating that skin tissue can tolerate prolonged MNs treatment without severe inflammatory responses (Figure 7d). Furthermore, the local irritation response of skin tissues after MNs treatment was conducted. The micropores in administration site of the skin almost completely disappear after 15 min, and return to its initial state within 30 min. There is no skin irritation response can be observed even after 24 h of MNs treatment, suggesting that long-term administration can be realized via MNs technology. Hence, these results further demonstrate the biosafety of the prepared MN patches for treatment *in vivo*.

Conclusions

In view of the limited pharmacodynamic window and side effects of conventional oral AP in the treatment of hyperuricemia, we developed a core-shell structured MNs system with programmed drug release functions to regulate serum uric acid levels for prolonged hyperuricemia management. The encapsulated AP in shell layer can be easily released, leading to a rapid decrease in SUA. The urate oxidase-calcium peroxide nanoparticles (UOx-CaO_2 NPs) can be slowly released from the core layer of MNs after exposure to skin tissue fluid, leading to the eliminate of existing uric acid and maintaining of a prolonged normouricemia state. *In vivo* results showed that the as-fabricated MNs exhibited an excellent anti-hyperuricemia effect to reduce SUA level to a normal state within 3 h and maintain normouricemia state for more than 12 h. In addition, This MNs treatment strategy could also effectively reduce the critical risk of liver and kidney damage. Thus, the core-shell structured MNs developed in this study are expected to be a new alternative for the exploration of clinical treatment of hyperuricemia.

Author Contributions

Rui Wang: Resources, Investigation, Data curation, Formal analysis, Visualization, Writing original draft. Yanfang Sun: Resources, Data curation. Han Wang: Validation, Writing-review & editing. Tianqi Liu: Validation, Writing-review & editing. Amin Shavandi: Writing-review & editing. Lei Nie: Validation, Writing-review & editing. Khaydar E. Yunusov: Resources, Data curation. Guohua Jiang: Methodology, Resources, Funding acquisition, Validation, Writing-review & editing.

Conflicts of interest

There are no conflicts to declare.

Acknowledgements

This work was supported by the Huadong Medicine Joint Funds of the Zhejiang Provincial Natural Science Foundation of China (LHDMZ23H300003) and National Natural Science Foundation of China (51873194).

References

1. M. Dehlin, L. Jacobsson, E. Roddy, *Nat. Rev. Rheumatol.* 2020, **16**, 380.
2. N. Dalbeth, A. L. Gosling, A. Gaffo, A. Abhishek, *Lancet* 2021, **397**, 1843.
3. J. Lu, N. Dalbeth, H.Y. Yin, C. G. Li, T. R. Merriman, W. H. Wei, *Nat. Rev. Rheumatol.* 2019, **15**, 413.
4. T. Petreski, R. Ekart, R. Hojs, S. Bevc, *Renal Failure* 2020, **42**, 978.
5. R. J. Johnson, G. L. Bakris, C. Borghi, M. B. Chonchol, D. Feldman, M. A. Lanaspa, T. R. Merriman, O. W. Moe, D. B. Mount, L. G. S. Lozada, E. Stahl, D. E. Weiner, G. M. Chertow, *Am. J. Kidney Dis.* 2018, **71**, 851.
6. D. W. Xie, Y. L. Shen, E. Z. Su, L. Du, J. L. Xie, D. Z. Wei, *Mol. Nutr. Food Res.* 2022, **67**, 2200162.
7. Z. R. Sun, H. R. Liu, D. Hu, M. S. Fan, M. Y. Wang, M. F. An, Y. L. Zhao, Z. M. Xiang, J. Sheng, *J. Agric. Food Chem.* 2021, **69**, 12741.
8. C. Liu, H. N. Zhou, R. R. Zhang, X. K. Wang, S. W. He, J. B. Zhang, X. Guo, Q. Wang, J. Y. Sun. *J. Funct. Foods* 2019, **61**, 103355.
9. Y. Tayama, K. Sugihara, S. Sanoh, K. Miyake, S. Kitamura, S. Ohta, *J. Pharm. Health Care* 2022, **8**, 31.
10. F. L. Li, Y. Y. Zhang, F. Wang, J. F. Chen, B. Wang, N. Li, X. H. Lin, J. Y. Zhuang, *New J. Chem.* 2022, **46**, 6852.
11. A. F. G. Cicero, F. Fogacci, M. Kuwabara, C. Borghi, *Med. Lith.* 2021, **57**, 1.
12. S. D. Beedkar, C. N. Khobragade, R. G. Bodade, A. S. Vinchurkar, *Comput. Biol. Med.* 2012, **42**, 657.
13. W. T. Crawley, C. G. Jungels, K. R. Stenmark, M. A. Fini, *Redox Biol.* 2022, **51**, 102271.
14. T. T. Cai, W. J. Zheng, Q. Chang, N. Li, J. L. Yanga, S. L. Hu, *J. Mater. Chem. A* 2022, **10**, 7792.
15. H. F. Wang, Y. S. Zhao, T. Y. Li, Z. Chen, Y. N. Wang, C. Y. Qin, *Chem. Eng. J.* 2016, **303**, 450.
16. W. Yang, J. W. Fei, W. Xu, H. Y. Jiang, M. Sakran, J. L. Hong, W. Y. Zhu, X. M. Zhou, *Colloid. Surface B* 2022, **212**, 112347.
17. X. Liang, Y. X. Chen, K. Wen, H. B. Han, Q. S. Li, *J. Mater. Chem. B* 2021, **9**, 6811.
18. T. Q. Liu, Y. F. Sun, G. H. Jiang, W. J. Zhang, R. Wang, L. Nie, A. Shavandi, K. E. Yunusov, U. E. Aharodnikau, S. O. Solomevich, *Acta Biomater.* 2023, **160**, 32.
19. A. Fang, Y. F. Wang, N. Y. Guan, Y. M. Zuo, L. M. Lin, B. J. Guo, A. Mo, Y. L. Wu, X. R. Lin, W. X. Cai, X. H. Wang, *Nat. Commun.* 2023, **14**, 4011.

20. Z. Y. Lu, S. Du, J. X. Li, M. Zhang, H. L. Nie, X. J. Zhou, F. L. Li, X. W. Wei, J. Q. Wang, F. Y. Liu, C. L. He, G. Yang, Z. Gu, *Adv. Mater.* 2023, 2303388.
21. T. T. Peng, Y. Y. Chen, W. S. Hu, Y. Huang, M. M. Zhang, C. Lu, X. Pan, C. B. Wu, *Engineering* 2023. DOI: https: 10.1016/j.eng.2023.05.009.
22. Y. Meng, X. J. Li, Y. Li, T. Y. Zhang, D. Liu, Y. Q. Wu, F. F. Hou, L. Ye, C. J. Wu, X. D. Feng, X. J. Ju, L. Jiang, *ACS Appl. Mater. Interfaces* 2023, **15**, 13892.
23. W. Chen, J. Wainer, S. W. Ryoo, X. Y. Qi, R. Chang, J. Li, S. H. Lee, S. Min, A. Wentworth, J. E. Collins, S. Tamang, K. Ishida, A. Hayward, R. Langer, G. Traverso, *Sci. Adv.* 2022, **8**, eabk1792.
24. L. J. Zheng, Y. Z. Chen, X. Gu, Y. Y. Li, H. Q. Zhao, W. J. Shao, T. Ma, C. B. Wu, Q. Q. Wang, *J. Control. Release* 2024, **365**, 274.
25. Z. C. Le, J. M. Yu, Y. J. Quek, B. Y. Bai, X. L. Li, Y. F. Shou, B. Myint, C. J. Xu, A. Tay, *Mater. Today* 2023, **63**, 137.
26. Z. H. Liu, Y. Wang, Y. H. Zhang, L. F. Hu, B. Z. Chen, Y. Li, X. D. Guo, B. R. Yu, F. J. Xu, *Bioact. Mater.* 2024, **33**, 497.
27. M. H. Lu, X. X. Zhang, L. J. Cai, J. J. Gan, J. L. Wang, Y. Wang, Y. J. Zhao, *Nano Today* 2024, **54**, 102072.
28. R. Wang, H. Wang, G. H. Jiang, Y. F. Sun, T. Q. Liu, L. Nie, A. Shavandi, K. E Yunusov, U. E. Aharodnikau, S. O. Solomevich, *Biomater. Sci.* 2023, **11**, 1704.
29. S. Z. Wu, B. Q. Qin, X. F. Tang, T. Cui, S. J. Yin, H. X. Dong, Y. J. Liu, S. Deng, H. Zhang, G. Y. Feng, H. Q. Xie, L. Lei. *Chem. Eng. J.* 2023, **466**, 143126.
30. L. Yan, A. P. Raphael, X. Y. Zhu, B. L. Wang, W. Chen, T. Tang, Y. Deng, H. J. Sant, G. Y. Zhu, K. W. Choy, B. K. Gale, T. W. Prow, X. F. Chen, *Adv. Healthc. Mater.* 2014, **3**, 555.
31. I. Guelcin, M. Oktay, E. Koeksal, H. Serbetci, S. Beydemir, O. I. Kuefrevioglu, *Asian J. Chem.* 2008, **20**, 2079.
32. M.H. Wang, J. M. Wu, H. C. Jiao, C. Oluwabiyi, H. F. Li, Ji. P. Zhao, Y. L. Zhou, X. J. Wang, H. Lin, *Free Radical Bio. Med.* 2022, **179**, 95.
33. S. Shen, M. Mamat, S. C. Zhang, J. Cao, Z. D. Hood, L. Figueroa-Cosme, Y. Xia, *Samll* 2019, **15**, 1902118.
34. Z. Y. Zeng, G. H. Jiang, Y. F. Sun, U. E. Aharodnikau, K. E. Yunusov, X. F. Gao, T. Q. Liu, S. O. Solomevich, *Biomater. Sci.* 2022, **10**, 5326.
35. W. Li, R. N. Terry, J. Tang, M. H. R. Feng, S. P. Schwendeman, M. R. Prausnitz, *Nat. Biomed. Eng.* 2019 **3,** 220.
36. J. W. Lee, J. H. Park, M. R. Prausnitz, *Biomaterials* 2008, **29**, 2113e.
37. P. Shi, R. Zhang, C. X. Liu, S. X. Wu, X. D. Pei, Y. Jiang, X. L. Liu, C. H. Wang, *J. Sci Food Agr.* 2022, **102**, 7079.
38. M. F. Wang, Z. Y. Hou, S. N. Liu, S. Liang, B. B. Ding, Y. J. Zhao, M. Y. Chang, G. Han, A. A. A. Kheraif, J. Lin, *Small* 2021, **17**, 2005728.
39. R. Dhouibi, H. Affes, M. Ben Salem, D. Moalla, R. Marekchi, S. Charfi, S. Hammami, Z. Sahnoun, K. Jamoussi, K. M. Zeghal, K. Ksouda, *Life Sci.* 2021, **268**, 118998.
40. R. Y. Wang, F. Lin, C. Ye, S. Aihemaitijiang, M. Halimulati, X. J. Huang, Z. Y. Jiang, L. T. Li, Z. F. Zhang, *Food Chem.* 2023, **399**, 133993.
41. L. H. Zhang, J. X. Liu, T. Jin, N. B. Qin, X. M. Ren, X. D. Xia, *Food Funct.* 2022, **13**, 12412.
42. Y. L. Liu, S. T. Gong, K. J. Li, G. Wu, X. H. Zheng, J. N. Zheng, X. W. Lu, L. Y. Zhang, J. C. Li, Z. R. Su, Y. H. Liu, J. H. Xie, J. N. Chen, Y. C. Li, *Biomed. Pharmacother.* 2022, **156**, 113941.
43. L. Y. Jiang, Y. L. Wu, C. Qu, Y. S. Lin, X. Q. Yi, C. J. Gao, J. Cai, Z. R. Su, H. F. Zeng, *Food Funct.* 2022, **13**, 10275.
44. L. J. Zhong, Y. S. Lin, S. T. Gong, X. Y. Wu, Y. H. Liu, J. N. Chen, Y. C. Li, F. Yan, Z. R. Su, Q. F. Xie, *Phytomedicine* 2023, **108**, 154521.
45. S. R. Han, R. R. Wei, D. R. Han, J. X. Zhu, W. Z. Luo, W. L. Ao, G. Y. Zhong, *Biomed. Res. Int.* 2020, **2020**, 2968135.
46. J. Maiuolo, F. Oppedisano, S. Gratteri, C. Muscoli, V. Mollace. *Int. J. Cardiol.* 2016, **213**, 8.
47. C. Stillhart, K. Vučićević, P. Augustijns, A. W. Basit, H. Batchelor, T. R. Flanagan, I. Gesquiere, R. Greupink, D. Keszthelyi, M. Koskinen, C. M. Madla, C. Matthys, G. Miljuš, M. G. Mooij, N. Parrott, A. L. Ungell, S. N. de Wildt, M. Orlu, S. Klein, A. Müllertz, *Eur. J. Pharm Sci.* 2020, **147**, 105280.
48. M. Y. Shen, T. I. Liu, T. W. Yu, R. Kv, W. H. Chiang, Y. C. Tsai, H. H. Chen, S. C. Lin, H. C. Chiu, *Biomaterials* 2019, **197**, 86.
49. B. Z. Chen, Y. T. He, Z. Q. Zhao, Y. H. Feng, L. Liang, J. Peng, C. Y. Yang, H. Uyama, M. A. Shahbazi, X. D. Guo, *Adv. Drug Delivery. Rev.* 2023, **203**, 115109.
50. J. H. Chen, P. T. Wu, C. C. Chyau, P. H. Wu, H. H. Lin, *J. Agric. Food Chem.* 2023, 71, 382.
51. L. Q. Xu, G.S. Lin, Q. X. Yu, Q. P. Li, L. T. Mai, J. J. Cheng, J. H. Xie, Y. H. Liu, Z. R. Su, Y. C. Li, *Front. Pharmacol.* 2021 **12**, 645879.
52. C. Deng, C. Y. Wang, W. P. Fu, L. J. Wu, Q. F. Jin, L. Zhang, W. Zhang, W. Li, M. X. Xie, *Mater. Design* 2023, **235**, 112415.
53. S. P. Jiang, W. Wang, J. M. Ke, S. Huang, J. Wang, C. X. Luo, X. X. Li, K. L. Zhang, H. H. Liu, W. S. Zheng, J. W. Zhang, C. Peng, *Biomater. Sci.* 2023, **11**, 1714.